IIETA International Information and Engineering Technology Association
Advancing the World of Information and Engineering

Journal Européen des Systèmes Automatisés
Vol. 59, No. 10, October, 2026, pp. 2893-2902
Journal homepage: http://iieta.org/journals/jesa

Power-Factor-Oriented Reactive-Power Control of a PV-Supported STATCOM under Sequential Load Variations

Abdulrahman Ali Khalaf[1*], Mohammed Y. Suliman[1], Mohamed Salem Mohamed Othman[2]

[1] Department of Electrical Engineering Techniques, Engineering Technical College, Northern Technical University, Mosul 41001, Iraq
[2] School of Electrical and Electronic Engineering, Engineering Campus, Universiti Sains Malaysia, Nibong Tebal 14300, Malaysia

Corresponding Author Email: abdulrahman.ali@ntu.edu.iq

Copyright: ©2026 The authors. This article is published by IIETA and is licensed under the CC BY 4.0 license (http://creativecommons.org/licenses/by/4.0/).

https://doi.org/10.18280/jesa.591011

Received: 5 August 2026
Revised: 6 October 2026
Accepted: 19 October 2026
Available online: 31 October 2026

Keywords:
power-factor reference generation, PV-supported STATCOM, reactive-power compensation, proportional-integral control, synchronous reference frame, source-current distortion

ABSTRACT

This paper evaluates a source-power-factor-oriented reactive-power reference for a photovoltaic (PV)-supported static synchronous compensator (STATCOM). The reference $Q_{s,ref} = 0.1425\ P_s$ targets power factor (PF) = 0.99 and is compared with a matched fixed-zero-Q proportional-integral (PI) benchmark targeting PF = 1.00 under balanced linear-load switching at 0.3, 1.0, and 1.4 s. The benchmark recovers faster after the two load connections (45.7 and 41.8 ms versus 65.8 and 68.9 ms) and reaches higher PF in all evaluated windows. It saturates at maximum load under the shared ±10 A reference limit; at ±15 A the proposed response is unchanged and the benchmark approaches unity PF (mean 0.999998 at maximum load). In matched ±15 A runs the 0.99 target required lower converter current (6.339 versus 10.745 A rms at 1.20–1.28 s). Source-current THD20 (about 1.1%) is not a controller advantage: the STATCOM-off baseline is near zero and the second harmonic depends on carrier phase and inner-loop sampling. In a passive resistive-capacitive (RC)-only run (voltage-source converter (VSC) isolated), source PF is already 0.984452/0.944331/0.984452 in the three windows, and the proposed converter current is only 1.139/1.170 A rms in the Load 2 and post-disconnection windows. Validation is simulation-based and limited to reactive-power control; nonlinear loads, experiments, and closed-loop DC-link regulation are not established.

1. INTRODUCTION

Photovoltaic (PV) integration motivates renewable-energy and power-quality assessment [1, 2]. This study evaluates source reactive-power control using a PV-supported compensator.

Converters and inductive loads motivate reactive-power regulation at the point of common coupling (PCC) [3, 4]. The validation uses balanced linear loads; its waveform indicators do not establish IEEE Std 519-2022 compliance [5].

A static synchronous compensator (STATCOM) supplies reactive current through a shunt voltage-source converter (VSC) [6]. PV-supported operation depends on implemented current references and direct-current (DC) control [7]. Here, PV and battery support the DC subsystem; complete energy management is not validated.

Recent studies address distinct objectives: active-current/feedforward PV-DSTATCOM control [7], renewable-energy power management [8], optimization-based maximum power point tracking (MPPT) with modified synchronous-reference-frame PV–battery control and real-time cases [9], and neuro-fuzzy unbalanced-voltage enhancement [10]. Liang et al. [11] assessed discrete-time deadbeat STATCOM control and parameter deviations; its coefficients require a discrete plant and delay model. Basnet and Roinila [12] experimentally combined proportional-integral (PI), deadbeat, and repetitive regulation for energy-storage-equipped STATCOM bandwidth and disturbance rejection. Li et al. [13] estimated voltage sensitivities online for adaptive reactive support under active-power–voltage coupling; their reduced-model results require electromagnetic-transient and hardware validation. Pandey et al. [14] investigated cascaded AC–DC voltage control for a PV-driven synchronverter, requiring DC coordination unlike the present zero d-axis reference.

Constant-power factor (PF), voltage–reactive-power (Volt–Var), active-power–reactive-power (Watt–Var) and constant-Q modes are established distributed-energy-resource functions in IEEE Std 1547-2018 [15]. Here, the PF target applies to source power, and the Q–P slope is fixed; voltage-dependent dispatch is not implemented. The 50-Hz simulation does not establish compliance with this 60-Hz interconnection standard.

Different objectives and validation conditions prevent direct performance comparisons. Here, $Q_{s,ref} = 0.1425\ P_s$ is compared with fixed-zero-Q control using the same plant, PI gains, limits and loads. The coefficient is fixed, without online gain or plant identification. Recovery, target errors and spectra document a bounded simulation contribution; different PF targets and current feasibility preclude universal-superiority claims.

2. PROPOSED PV-STATCOM SYSTEM CONFIGURATION

The balanced 380-V/50-Hz network supplies constant-impedance inductive loads. The shunt VSC connects through two resistive-inductive (RL) sections and a shunt resistive-capacitive (RC) branch; PV, perturb-and-observe (P&O) boost and battery support its DC side (Figure 1).

The controller receives source active and reactive powers, PCC voltages, converter currents, and the angle from a phase-locked loop (PLL). Source power measurements are averaged over one 50-Hz cycle before feedback. Load 2 connects at 0.3 s; Load 3 connects at 1.0 s and disconnects at 1.4 s. Source-power-factor results therefore include the dynamics of the measurement filters.

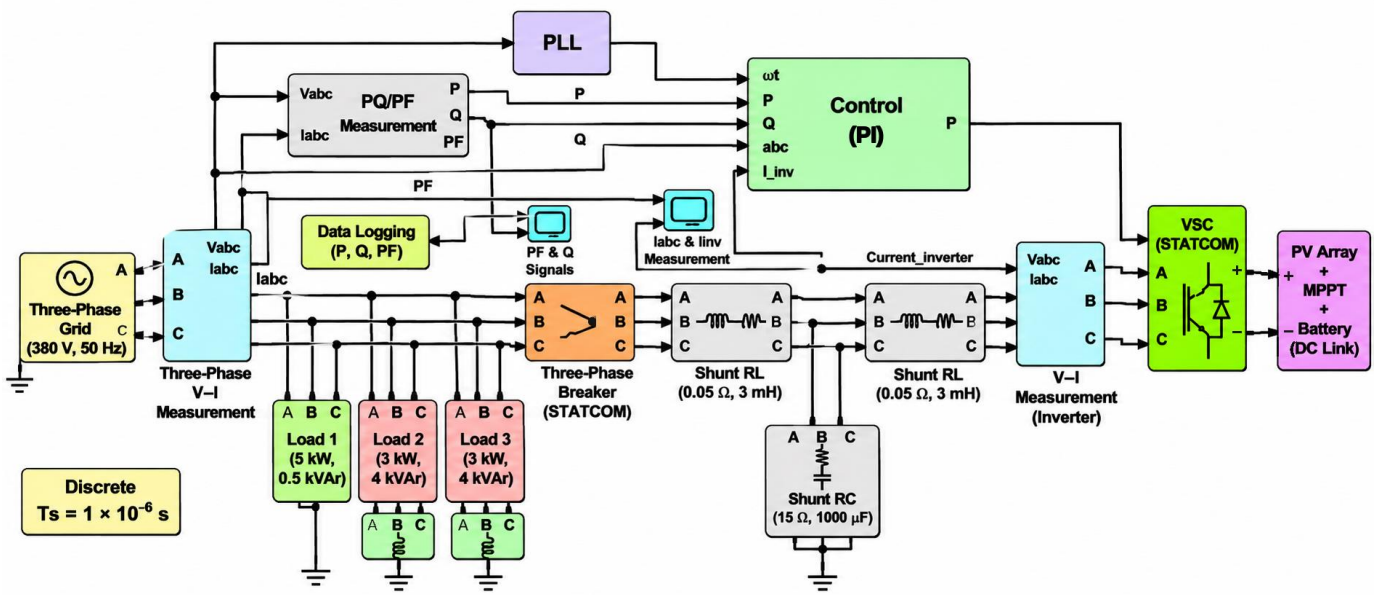


Figure 1. Complete MATLAB/Simulink model of the proposed grid-connected PV-STATCOM system under sequential load switching

2.1 Operating principle

Figure 2 identifies the VSC and supporting DC subsystem. The converter is evaluated with zero d-axis current reference and an outer reactive-power loop. General active/reactive current-reference inversion and energy-management functions are not used in this operating mode. The reference-generation equations are stated once in Section 4, and their implementation is detailed in Section 5.

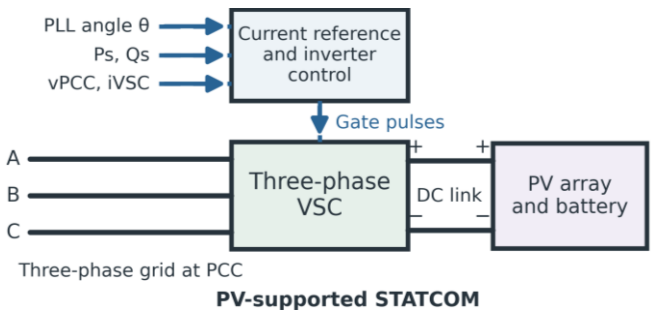


Figure 2. Functional overview of the implemented PV-supported STATCOM and its shared PV-battery DC link

The modulation commands use a fixed gain of 2/800 rather than measured-DC-voltage normalization or a closed-loop DC-voltage PI regulator. Accordingly, 800 V is a normalization base, not a demonstrated regulated DC-link setpoint. Battery and PV voltage dynamics remain a validation limitation.

3. SUPPORTING PHOTOVOLTAIC-BATTERY SUBSYSTEM

The supporting DC subsystem comprises a PV array, a P&O-controlled boost converter, DC capacitance and a nickel–cadmium battery (Figure 3). Irradiance primarily affects PV current, while temperature affects maximum-power-point voltage [16, 17]. Its settings are retained in both controller cases; PV-energy performance is not the comparison objective.

3.1 Photovoltaic-array configuration

The implemented PV array contains 20 parallel strings, each comprising 20 series-connected modules. Each module consists of 60 PV cells and has a rated maximum power of 213.15 W, an open-circuit voltage of 36.3 V, a short-circuit current of 7.84 A, a maximum-power-point voltage of 29 V, and a maximum-power-point current of 7.35 A.

The total number of PV modules is:

$$N_{\mathrm{PV}} = 20 \times 20 = 40 \tag{1}$$

The total installed PV capacity is:

$$P_{\mathrm{PV,rated}} = 400 \times 213.15 = 85.26\,\mathrm{kW} \tag{2}$$

The maximum-power-point voltage of the complete array is:

$$V_{\mathrm{mpp,array}} = 20 \times 29 = 580\,\mathrm{V} \tag{3}$$

The corresponding maximum-power-point current is:

$$I_{\text{mpp,array}} = 20 \times 7.35 = 147 \text{ A} \quad (4)$$

The corresponding array open-circuit voltage and short-circuit current are 726 V and 156.8 A, respectively. These values are calculated directly from the PV-module parameters implemented in the MATLAB/Simulink model.

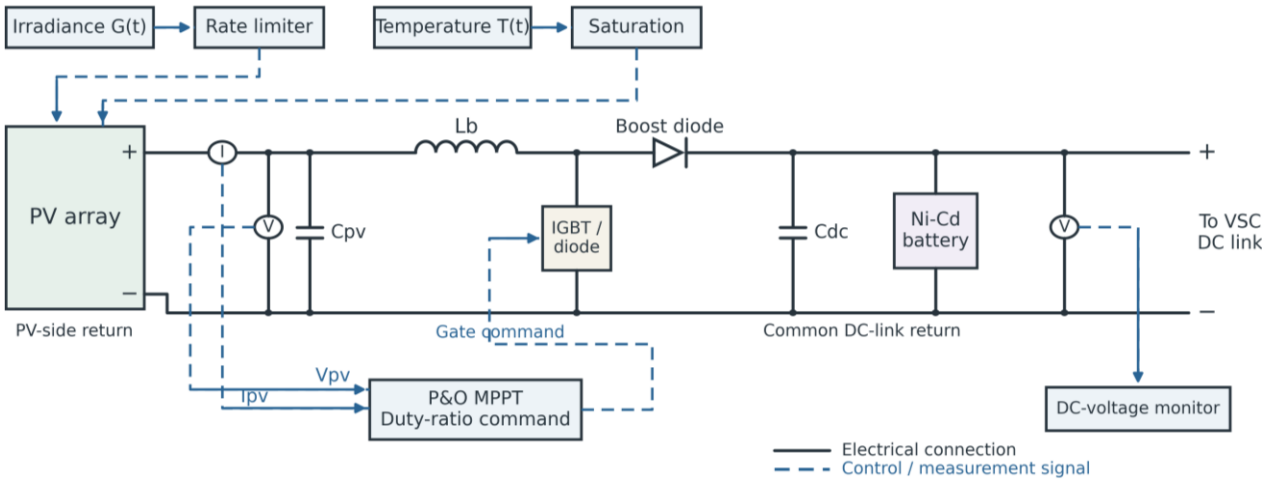


Figure 3. Schematic of the implemented PV-battery subsystem with P&O MPPT, boost conversion, and DC-link monitoring
Note: PV = photovoltaic, P&O = perturb-and-observe, MPPT = maximum power point tracking, DC = direct current.

3.2 Irradiance and temperature profiles

Table 1 gives the shared irradiance/temperature commands. Irradiance slew is ±6000 W/m²/s and temperature bounds are 5–55 ℃. The final command at 2.0 s has no subsequent evaluated response. Separate irradiance sensitivity and MPPT efficiency are unverified.

Table 1. Applied irradiance and Photovoltaic (PV) cell temperature profiles

Time (s)	Irradiance $(\mathbf{W/m^2})$	PV-Cell Temperature (℃)
0.0	1000	25
0.6	400	35
1.2	600	40
1.6	800	45
2.0	1000	50

3.3 Perturb and observe maximum power point tracking algorithm

Fixed-step P&O compares filtered PV power and voltage with their previous samples to update boost duty ratio [18, 19]:
The instantaneous PV power at the sampling instant k is:

$$P_{\text{PV}}(k) = V_{\text{PV}}(k) I_{\text{PV}}(k) \quad (5)$$

The changes in PV power and voltage are:

$$\Delta P(k) = P_{\text{PV}}(k) - P_{\text{PV}}(k-1) \quad (6)$$

$$\Delta V(k) = V_{\text{PV}}(k) - V_{\text{PV}}(k-1) \quad (7)$$

The implemented perturbation direction is:

$$s(k) = \begin{cases} -1, & \Delta P(k)\Delta V(k) > 0, \\ +1, & \Delta P(k)\Delta V(k) < 0, \\ 0, & \Delta P(k)\Delta V(k) = 0. \end{cases} \quad (8)$$

The duty ratio is updated as:

$$D(k) = D(k-1) + s(k)\Delta D \quad (9)$$

The fixed perturbation step implemented in the controller is:

$$\Delta D = 0.0005 \quad (10)$$

The duty command is saturated before boost switching.

3.4 Direct-current-direct-current boost-converter configuration

The boost converter uses an insulated-gate bipolar transistor (IGBT), diode, inductor and capacitor; P&O adjusts PV operating voltage through its duty command [6].
For ideal continuous conduction, the voltage relation is:

$$V_{dc} = \frac{V_{PV}}{1 - D} \quad (11)$$

where, D is duty ratio; equivalently:

$$D = 1 - \frac{V_{PV}}{V_{dc}} \quad (12)$$

The averaged continuous-conduction dynamics are:

$$L_b \frac{di_L}{dt} = V_{PV} - (1 - D)V_{dc} \quad (13)$$

The corresponding DC-node equation is:

$$C_b \frac{dV_{dc}}{dt} = (1 - D)i_L - i_{dc} \quad (14)$$

L_b is boost inductance; C_b is DC-side capacitance; i_L and i_{dc} are inductor and net DC-node currents.
The boost parameters are L_b = 0.8 mH, PV-side capacitance 2 mF, DC-side capacitance 300 μF and IGBT on-state resistance 1 mΩ. Its carrier is 3 kHz; MPPT inputs are sampled at 100 μs. The power-system step is 1 μs, distinct from control

sampling.

3.5 Battery configuration

The nickel–cadmium battery is rated 700 V/700 Ah (nominal energy 490 kWh), with an initial SOC of 100%, a response-time parameter of 30 s and a configured full-charge voltage of 800.922 V. These capacity settings are inherited from the base model and are not optimized; they are large relative to the 85.26 kW PV array and the connected loads. The 2 s simulation does not assess SOC management or long-duration energy balance.

4. POINT OF COMMON COUPLING POWER CALCULATION AND POWER-FACTOR REFERENCE FORMULATION

The feedback block calculates instantaneous three-phase power from PCC voltages and source currents, then applies one-cycle moving averages. Under the adopted amplitude-invariant synchronous-reference-frame convention, the corresponding power relationships are [6]:

$$P_s = \frac{3}{2}\left(v_d i_{sd} + v_q i_{sq}\right) \tag{15}$$

$$Q_s = \frac{3}{2}\left(v_q i_{sd} - v_d i_{sq}\right) \tag{16}$$

where, v_d and v_q are the synchronous-reference-frame components of the PCC voltage, while i_{sd} and i_{sq} are the corresponding source-current components.

The source power factor is calculated as:

$$PF_s = \frac{|\,P_s\,|}{\sqrt{P_s^2 + Q_s^2}} \tag{17}$$

The selected source power-factor reference is:

$$PF_{\text{ref}} = 0.99 \tag{18}$$

The corresponding reactive-power coefficient is:

$$\tan[\cos^{-1}(0.99)] \approx 0.1425 \tag{19}$$

Accordingly, the reactive-power error implemented in the MATLAB/Simulink control model is:

$$e_Q = Q_s - 0.1425 P_s \tag{20}$$

The error e_Q is processed by the outer PI controller to produce the q-axis current reference. The coefficient 0.1425 approximates tan(arccos(0.99)); it is constant, whereas its product with measured source active power changes with operating condition. For positive P_s, the positive source-Q target denotes lagging PF = 0.99; the P-Q magnitude alone does not encode leading/lagging sign. The formulation assumes the tested positive-active-power, inductive-load regime; reverse-flow operation is not validated. The reported PF is the P-Q-based indicator |P|/sqrt(P²+Q²), not a separate broadband true-power-factor measurement under distorted conditions.

5. IMPLEMENTED REACTIVE-POWER CONTROL OF THE PV-SUPPORTED STATCOM

Measured source powers, PCC voltages, converter currents and PLL angle feed the cascaded reactive-power and current loops. PCC voltages and converter currents are transformed into synchronous-frame components [6, 9, 11]. Figure 4 shows the control signal flow.

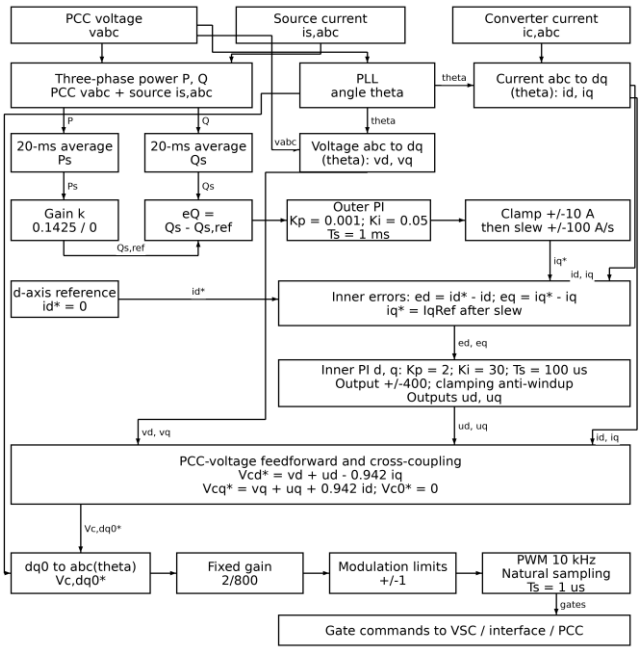


Figure 4. Control signal flow with connected PCC/source measurements, PLL angle, converter-current feedback, PI loops, feedforward, and PWM

Note: Proposed/Fixed-Q use k = 0.1425/0; baseline limits are ±10 A and ±100 A/s; point of common coupling (PCC); phase-locked loop (PLL); proportional-integral (PI); pulse-width modulation (PWM).

The signal path is measured source active power → coefficient 0.1425 → source Q reference, followed by subtraction from measured source Q. In the fixed-reference benchmark, only this coefficient is changed to zero. The same PI controllers remain active in both runs.

The discrete outer PI uses $K_{p,Q} = 0.001$, $K_{i,Q} = 0.05$, and $T_{s,Q} = 1$ ms. Its baseline output is limited to ±10 A, followed by a ±100-A/s rate limiter producing the q-axis current reference.

In the implemented reactive-compensation mode, the d-axis current reference is set to zero:

$$i_d^* = 0 \tag{21}$$

The d- and q-axis current-tracking errors are calculated as:

$$e_d = i_d^* - i_d \tag{22a}$$

$$e_q = i_q^* - i_q \tag{22b}$$

where the measured converter-current components provide the inner-loop feedback. Both d- and q-axis current errors are processed by discrete PI controllers having $K_{p,c} = 2$, $K_{i,c} = 30$, a sample time of 100 μs, output limits of ±400, and clamping anti-windup.

PCC-voltage feedforward and cross-coupling combine with the current-PI outputs. Each interfacing RL section has R_f =

0.05 Ω and L_f = 3 mH; $\omega L_f \approx 0.942$ at 50 Hz. The implemented voltage references are:

$$V_{cd}^{*} = V_d + u_d - 0.942 i_q \quad (23)$$

$$V_{cq}^{*} = V_q + u_q + 0.942 i_d \quad (24)$$

where, u_d and u_q are the outputs of the corresponding discrete current controllers, while v_d and v_q are the synchronous-frame PCC-voltage components. The implemented cross-coupling coefficient is:

$$\omega L_f = 0.942 \quad (25)$$

The measured converter current is positive from converter to PCC. The amplitude-invariant abc → dq transformation uses the same PLL angle for voltage and current, with the selected alignment 90 degrees behind the phase-A axis. Reconstruction from recorded abc signals reproduces the logged dq components. In the recorded frame, v_d is negative, and v_q is approximately zero; thus, positive i_q gives positive injected $Q_{conv} = -1.5\, v_d\, i_q$. Eqs. (23) and (24) are retained.

The zero-sequence reference-voltage component is set to:

$$V_{c0}^{*} = 0 \quad (26)$$

PLL-based dq0-to-abc transformation, fixed gain 2/800 = 0.0025 and ±1 limiting generate commands for natural-sampling two-level pulse-width modulation (PWM), with 10 kHz carrier and 1 µs PWM sampling. The q reference responds to source power; the d reference remains zero. Consequently, these results validate neither controlled PV active-power injection nor closed-loop DC-link regulation.

5.1 Parameter selection and stability scope

Table 2 summarizes the controller and interfacing parameters. The PI gains were empirically adjusted. The decoupled approximation G(s) = 1/(L_f s + R_f), with L_f = 3 mH and R_f = 0.05 Ω, gives K_p = 1.885 and K_i = 31.416 for a nominal 100-Hz design target, close to the implemented 2 and 30. K_i/K_p = 15 s⁻¹ differs from R_f/L_f = 16.667 s⁻¹; cancellation is inexact. This target is 1/100 of the 10 kHz carrier, not a measured full-system bandwidth. The outer gains (0.001, 0.05; 1 ms sampling) remain empirical and identical in both cases. With unity negative feedback, the reduced characteristic is:

$$L_f s^2 + (R_f + K_p)s + K_i = 0 \quad (27)$$

For the implemented gains:

$$0.003 s^2 + 2.05 s + 30 = 0 \quad (28)$$

Its roots are −668.372 and −14.962 s⁻¹. Both are negative, establishing stability only for this continuous-time approximation. The corresponding open-loop is:

$$L(s) = \frac{K_p + K_i/s}{L_f s + R_f} \quad (29)$$

The reduced open-loop crossover is 666.627 rad/s (106.097 Hz), with 90.143° continuous-time phase margin. The estimated computation delay of 100 µs, and zero-order hold delay of 50 µs, result in an effective delay of 150 µs and a remaining angle of 84.414° (or 85°). This delay is not identified from the implementation. The approximation does not include the second RL section, RC branch, PLL, outer loop, switching and nonlinear limits; thus, it does not include any full model margin or global robustness. If this converter-to-PCC path is assumed to be made up of both RL sections (L = 6 mH and R = 0.1 Ω), the same gains result in a pair of poles at −326.3 and −15.3 s⁻¹, and the same assumed delay of 150 µs gives a crossover near 53 Hz and about 86° phase margin, so the 100-Hz design target only applies to the single-section approximation.

Table 2. Controller and interfacing parameters verified from the implemented MATLAB/Simulink model

Parameter	Implemented Value	Function/Location
Target source power factor	0.99	Source Q reference
Reactive-power coefficient	0.1425	Q error gain
Reactive-power proportional-integral (PI)	K_p = 0.001; K_i = 0.05; T_s = 1 ms	Outer q-axis reference loop
Reactive-current reference limits	±10 A; slew ±100 A/s	PI output and rate limiter
d-axis current reference	0 A	Reactive-compensation mode
d/q current PI controllers	K_p = 2; K_i = 30; T_s = 100 µs	Inner current loops
Current-PI output limits	±400; clamping	Clamping anti-windup
Interfacing branch	R = 0.05 Ω; L = 3 mH	Per phase
Cross-coupling gain	0.942	50-Hz operation
Voltage normalization	2/800 = 0.0025	Fixed modulation scaling
Modulation saturation	±1	Before pulse-width modulation (PWM)
PWM generator	10 kHz; T_s = 1 µs	Natural sampling, two-level
Phase-locked loop (PLL) PI controller	K_p = 222; K_i = 24650; T_s = 10 µs	Output limiting disabled
Power-system discrete step	1 µs	powergui

The implementation scope and physical parameters are described below. The implementation scope and physical parameters are described below.

Table 3 gives the electrical settings. The source is 380 V/50 Hz with a short-circuit level of 100 MVA and it is a stiff-source test. Each 3 kW/4 kVAr load has nominal PF = 0.60. The two 3-mH RL sections give a total of 1.885 Ω of reactance (per phase) at 50 Hz. The power absorption and dissipation of the measured PCC branch differs from rated load sums since the RC branch is a 15 Ω, 1000 µF RC branch and not optimized for resonance and damping.

If amplitude is not important in the dq scaling, i_d^{*} = 0 and $|i_q^{*}| <= 10$A are equivalent to 7.071A root mean square (RMS). At 380 V, the nominal control-derived base is √3 × 380 × 7.071 = 4.654 kVA, approximately 4.654 kVAr for reactive current. This is an estimate of the nominal voltage (not a transient bound or a hardware rating) that is sinusoidal. The bridge modeled does not have a nameplate of kVA; in practice,

thermal and protection margins must be considered.

Table 3. Electrical model parameters

Parameter	Value
Grid	380 V line-line RMS; 50 Hz
Source impedance setting	100 MVA short-circuit level; X/R = 7
Base load	5 kW; 0.5 kVAr at nominal voltage
Load 2 and Load 3	Each 3 kW; 4 kVAr at nominal voltage
Load representation	Balanced constant impedance
Two series resistive-inductive (RL) sections	Each R = 0.05 Ω; L = 3 mH per phase
Shunt series resistive-capacitive (RC) branch	R = 15 Ω; C = 1000 μF per phase
PV array	20 parallel × 20 series modules; 85.26 kW
Array MPP at module rating	580 V; 147 A
Boost stage	0.8 mH; 3 kHz; IGBT Ron = 1 mΩ
PV-side/DC-side capacitors	2 mF/300 μF
Battery	NiCd; 700 V; 700 Ah; initial SOC 100%
Battery nominal energy	490 kWh; response parameter 30 s
VSC bridge	Three-arm IGBT/diode; Ron = 1 mΩ
DC normalization base	800 V; fixed gain 0.0025
VSC hardware nameplate	Not specified by the modeled bridge
Control-derived AC base	4.654 kVA at 380 V; $i_d^* = 0$; $\lvert i_q^* \rvert \le 10$ A (7.071 A RMS); modulation ±1
Simulation duration/step	2 s/powergui discrete step 1 μs

It is suitable for boosting to the 700 V nominal battery voltage or for an 800 V modulation base with the 580 V PV MPP. The voltage required for sinusoidal PWM interfacing is approximately 621 V DC for 380 V line-to-line interfacing. The 0.1–2.0 s DC ranges are 802.337–805.823 V (Proposed) and 802.360–805.851 V. (Fixed-Q), i.e. non-regulated. The 11-kW nominal load dictates PV/storage array sizing. The 300 μF capacitor stores 96 J at 800 V, with no documentation of original stress, ripple, or sizing criteria.

The RC branch analytically has 9.212 kW/−1.955 kVAr at nominal branch voltage of 380 V. Before network effects, the maximum loading would result in the following values: P ≈ 20.212 kW and Q ≈ 6.545 kVAr. Proposed/Fixed-Q nominal compensation is 3.665/6.545 kVAr, or 7.875/14.064-A dq amplitudes. The 14.064-A estimate does not account for reactive consumption in the RL sections (analytically $3\omega L \cdot I^2$ ≈ 0.33 kVAr per 3-mH section at 10.745 A rms), but this is not the whole reason for the difference; it is not a measured ceiling. F20 logs reach 17.300 A before slew and 16.923 A after slew. The 7.875 A estimate is not a measured reference maximum of 8.789 A at 1.20–1.28 s or 9.526 A over the whole run, but is a phase RMS current estimate.

6. SIMULATION RESULTS AND DISCUSSION

6.1 Benchmark protocol and performance definitions

In both cases, the network, loads, environmental inputs, PI gains, initial conditions, and limits are identical, with compensation. Connected at initialization, Proposed uses $Q_{s,ref}$ = 0.1425 P_s (PF target 0.99); Fixed-Q uses $Q_{s,ref}$ = 0 (target 1.00). This is a comparison of reference policies in a single PI architecture. The tracking metrics should be interpreted in the context of the different targets. Table 4 lists the load sequence. Tables 5-7 and regenerated Figures 5-7 use the same unified recorded runs for each controller, with Breaker1 closed at initialization (switching time [10] s, external control off), verified before and after each 0–2 s simulation; the power and source-current records reproduce the current Tables 5 and 6 dataset exactly.

Table 4. Nominal connected-load totals and event sequence

Interval (s)	P (kW)	Q (kVAr)	Load Power Factor (PF)
0–0.3	5	0.5	0.9950
0.3–1.0	8	4.5	0.8716
1.0–1.4	11	8.5	0.7913
1.4–2.0	8	4.5	0.8716

Table 4 lists rated load-block sums, excluding the RC branch and other network power exchanges. The load PF is an analytical value from P/sqrt(P^2+Q^2), not a measured uncompensated-source baseline. Load 3 adds 4 kVAr, the same nominal reactive demand as Load 2. The original 0.4-kVAr Load 3 entry was a typographical error; its implemented 4 kVAr demand gives 8.5 kVAr and PF ≈ 0.791 at maximum load, replacing 4.9 kVAr and 0.913.

Recovery is the first entry into $|PF - PF_{ref}| \le 0.01$ sustained for 20 ms, before the next event/end; it is not the asymptotic settling time. Steady-state mean absolute error (MAE) is mean($|PF - PF_{ref}|$), and signed error is mean($PF - PF_{ref}$), over 0.70–0.78, 1.20–1.28 and 1.80–1.88 s. Maximum upward/downward deviations are 100 max(0, max($PF - PF_{ref}$)) and 100 max(0, max($PF_{ref} - PF$)), in PF percentage points (pp), not relative overshoot. Invalid startup PF samples are excluded.

6.2 Dynamic comparison

After connecting Load 2 and Load 3, respectively, the proposed recovery method recovers the original load, while Fixed-Q recovers only the previous load, requiring 45.7 and 41.8 ms. The minimum compensated PF values implied by the downward deviations are about 0.95378/0.95827 for Proposed and 0.98198/0.98492 for Fixed-Q. The compensated responses are not equal to the nominal uncompensated load PF values of Table 4. Table 5 and Figure 5 report the recovery times.

Table 5. Dynamic metrics relative to each controller target

Controller	Event	Rec. ms	Above pp	Below pp
Proposed	L2 on	65.8	0.279	3.622
Proposed	L3 on	68.9	0.067	3.173
Proposed	L3 off	0.0	1.000	0.090
Fixed-Q	L2 on	45.7	0.000	1.802
Fixed-Q	L3 on	41.8	0.000	1.508
Fixed-Q	L3 off	0.0	0.000	0.697

Proposed: source PF target 0.99; Fixed-Q: fixed source-Q reference of zero, with PF target 1.00. Both use identical PI loops. A displayed recovery of 0.0 ms means the criterion was already met at the start of the event window; it implies neither instantaneous physical response nor Q settling.

After Load 3 is disconnected, the proposed PF briefly rises toward unity (1.000-pp upward deviation, Table 5) and returns

to about 0.99. The 1.000-pp upward deviation is an excursion from the selected reference, and not necessarily harmful degradation in PF. Figure 6 shows a temporary negative excursion of the source-Q. From PF magnitude alone, it is not possible to determine whether it is leading or lagging reactive-power exchange.

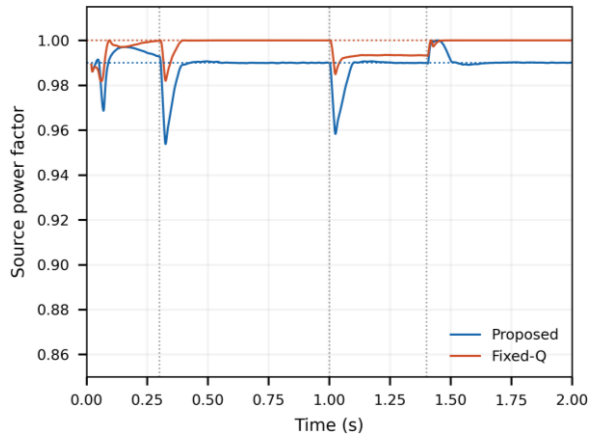


Figure 5. Source power factor (PF) for the proposed and fixed-Q-reference PI cases

Note: Dotted horizontal lines show their different targets; vertical lines indicate load events. Regenerated from the same recorded runs used for Tables 5–7.

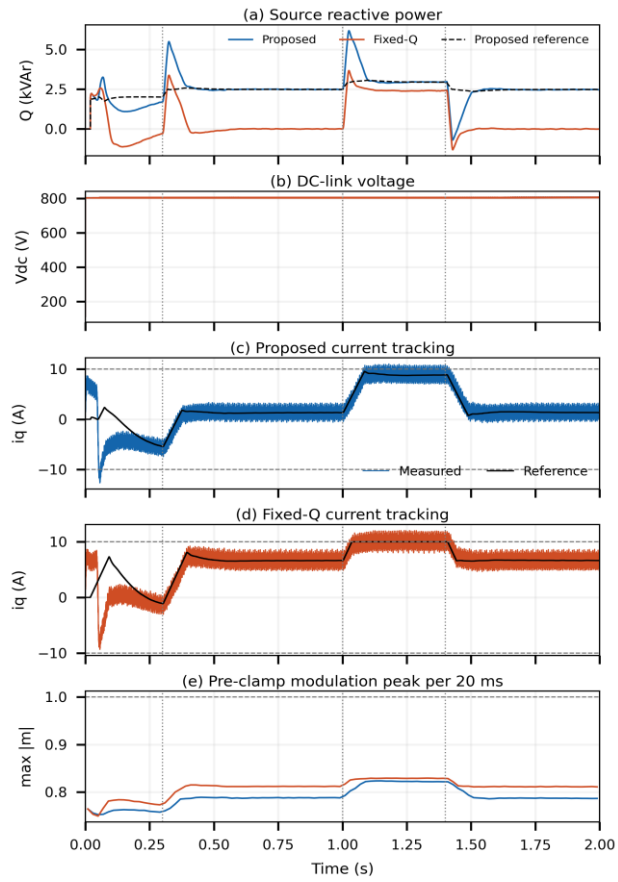


Figure 6. Simulated power and control diagnostics. (a) Source reactive power, Q (kVAr) (b) DC-link voltage, Vdc (V) (c) Proposed current tracking (d) Fixed-Q current tracking: dashed lines are reference limits for ±10 A (e) Maximum absolute modulation of the pre-clamp across phases for every 20 ms interval

Note: Vertical dotted lines mark load events. Reconstructed from the combined runs in Tables 5–7.

Fixed-Q has lower MAE in two windows and Proposed in the L3-on window; Fixed-Q has higher PF in all three windows; Mean MAE: 1.1221e-04/0.002197 for Proposed/Fixed-Q. Figure 6 uses 10 µs internal logs: at 1.20–1.28 s, pre-slew near-limit occupancy is 0%/100%, maximum $|i_q^*|$ is 8.789/10.000 A, and mean PF is 0.990148/0.993409. Overall near-limit occupancy over 0.1–2.0 s is 0%/20.58%; sampled modulation stays within ±1. These traces support a reference-feasibility constraint, not semiconductor-current protection, internal anti-windup-state measurement or control-law superiority. Near-limit occupancy counts pre-slew references within 0.001 A of +10 A, rather than exact saturation. Table 6 reports the MAE.

Pre-slew outer-PI occupancy uses 10-µs samples over 0.1–2.0 s (20.58%, ≈391 ms); Table 8 uses 1-ms post-slew intervals over 0–2 s (F10: 370 ms). Different signals, windows and sampling, together with slew-delayed bound entry/exit, prevent direct equivalence.

Table 6. Metrics of power factor (PF) tracking at steady state

Controller	Event	MAE	Signed Error	Mean PF
Proposed	L2 on	6.36e-05	-6.08e-05	0.98994
Proposed	L3 on	0.000178	+0.000148	0.99015
Proposed	L3 off	9.53e-05	+9.53e-05	0.99010
Fixed-Q	L2 on	1.57e-07	-1.57e-07	1.00000
Fixed-Q	L3 on	0.006591	-0.006591	0.99341
Fixed-Q	L3 off	2.30e-07	-2.30e-07	1.00000

6.3 Source-current harmonic assessment

Identical 80 ms, four-cycle fast Fourier transform (FFT) windows use uniformly spaced samples, omit the duplicate endpoint and remove mean current. Total harmonic distortion through order 20 (THD20) is 100 times the root-sum-square of orders 2–20 divided by the 50 Hz fundamental amplitude. Higher orders, interharmonics and the 10 kHz switching band are excluded. Both controllers use the same routine; Table 7 lists phase values and their arithmetic mean.

Table 7. Source-current THD20 (%) by controller and phase

Controller	Window (s)	Phase A	Phase B	Phase C	Mean
Proposed	0.70–0.78	0.9577	1.1141	1.2820	1.1179
Proposed	1.20–1.28	0.9502	0.9979	1.0684	1.0055
Proposed	1.80–1.88	0.9542	1.0623	1.3571	1.1245
Fixed-Q	0.70–0.78	1.3203	1.1996	1.2828	1.2676
Fixed-Q	1.20–1.28	1.0230	0.8986	1.0617	0.9944
Fixed-Q	1.80–1.88	1.2610	1.2698	1.3070	1.2793

Figure 7 retains orders 2–20: Phase-A H2 is 0.8441%/1.2656%, and H4 is 0.3681%/0.2125% for Proposed/Fixed-Q. Table 7 shows that after disconnection, Proposed THD20 is higher than baseline, while Fixed-Q is lower than baseline after the connection of Load 3. These residual spectra do not prove selective mitigation [20] nor gives any indication of superior control. OFF disconnects VSC and RC; its THD20 is 0.000103/0.000066/0.000083%. Separate ±15 A means are 1.082647%/1.229871%. Even though the PLL with 50Hz is stable, voltage H2 and unclipped modulation are negligible; H2 still persists with shifted and 1–8-cycle windows and direct projection, before PWM. The proposed inner sampling time at ±100 µs gives the highest values for H2/THD20 (Supplement to Table 7) when

compared with three tested phases (90°, ±100-µs and ±150-µs). At 90°, 50-µs sampling gives H2 = 0.14689%, THD20 = 0.38103% and PF ≈ 0.99; orders 3–20 remain similar (0.33608%/0.34342% at 100/50 µs). Unchanged gains establish timing sensitivity, not a unique cause. Table 7 and Figure 7 retain the 90° baseline; a matched 0° comparison would require rerunning both policies.

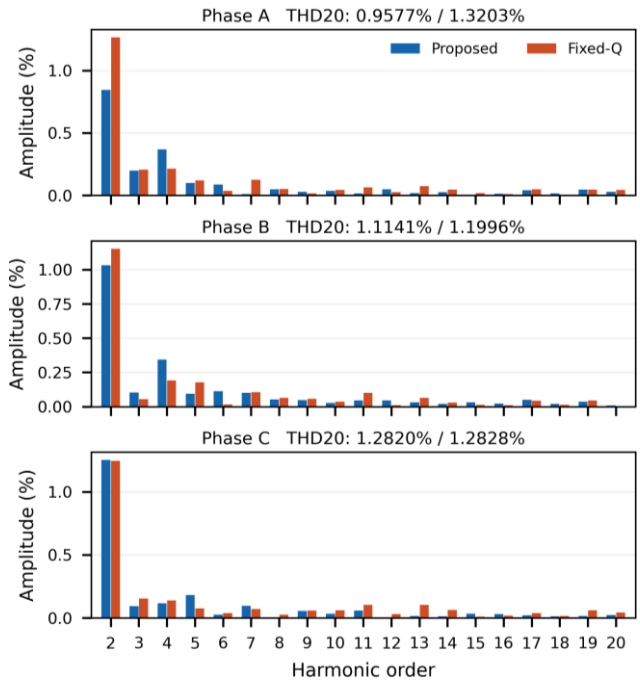


Figure 7. Source-current harmonic orders 2–20 at 0.70–0.78 s; amplitudes are normalized to each phase's fundamental. Panel values list proposed/Fixed-Q THD20
Note: Regenerated from the same recorded runs used for Tables 5–7.

Table 8. Timing diagnostics for the proposed ±15 A/S100 scheme; arithmetic mean across three phases and three four-cycle windows, inner sampling 100 µs

Carrier Phase (°)	Mean H2 (%)	Mean THD20 (%)
90	1.02368	1.08265
0	0.18892	0.29722
180	0.17863	0.28731

Table 9. Reference constraints and maximum-load means

Case	Slew (A/s)	Peak (A)	At Limit (ms)	Mean Power Factor (PF)	Mean Q (kVAr)
P10	100	9.526	0	0.990027	2.943
F10	100	10.000	370	0.993364	2.396
P15	100	9.526	0	0.990027	2.943
F15	100	15.000	185	0.999998	0.031
P15	500	8.871	0	0.989901	2.967
F15	500	15.000	163	0.999998	0.037
P15	2000	8.871	0	0.989901	2.967
F15	2000	15.000	165	0.999998	0.030
F20	100	16.923	0	0.999993	−0.045

THD20 is a qualitative indicator of the quality of the waveform. Additionally, the short simulation windows and twentieth-order cutoff in IEEE Std 519-2022 [5] are not sufficient to fully satisfy PCC harmonic assessment requirements. A total demand distortion (TDD) by current demand or a current limit category and/or compliance duration assessment is not provided. There is no claim for certification or a universal 5% current-THD threshold.

6.4 Current limits

Eight ±10/±15 A runs test 100/500/2000 A/s slew; an additional F20 diagnostic uses ±20 A, slew 100 A/s over 0–2 s. Bound duration sums 1-ms intervals with a post-slew reference that is within 10^{-6} A of the bound. The At Limit durations in Table 9 are calculated over 0–2 s.

P/F and 10/15/20 are Proposed/Fixed-Q and the ampere bounds, respectively. Proposed records coincide at slew 100 A/s for ±10/±15 A and at 500/2000 A/s (peak slope 266.039 A/s). F15 reaches 15 A for 185/163/165 ms and is not unconstrained. F20 peaks at 16.923 A after slew (17.300 A before); 1 ms logs show zero bound occupancy and mean PF/Q = 0.999993/−0.045 kVAr. This is the feasibility of logging references, not protection on the spot. Figure 8 shows the recorded current-reference and measured-current traces. Table 10 reports PF recovery and Q settling times for the ±15 A cases.

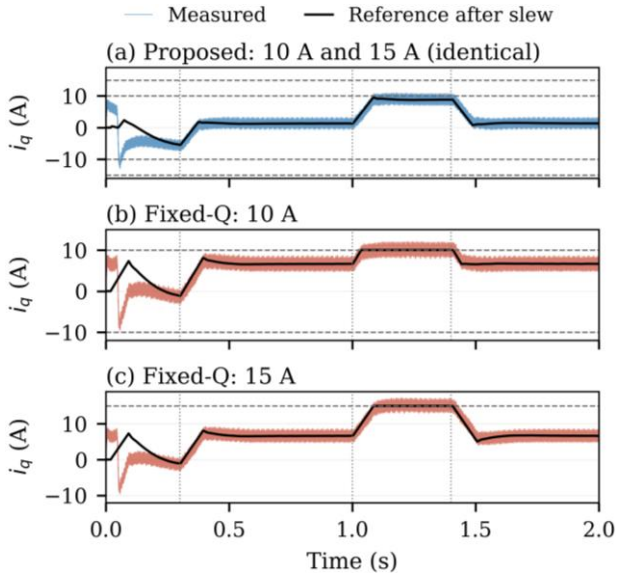


Figure 8. Original logged IqMeasured and post-slew IqRef, at ±10/±15 A reference limits, at 100 A/s

Table 10. Power factor (PF) recovery times (ms, L2/L3/D) and Q settling times (ms) for the ±15 A cases at different slew rates

Case/ Slew	PF rec. L2/L3/D	Q Settle L2	Q Settle l3	Q Settle d
P15/500	57.7/55.4/0.0	149.4	163.8	174.3
P15/2000	57.7/55.4/0.0	149.4	163.8	174.3
F15/500	30.0/0.0/0.0	148.7	392.3	165.0
F15/2000	30.0/0.0/0.0	149.7	149.8	165.3
P15/100	65.8/68.9/0.0	199.8	188.0	192.0
F15/100	45.7/41.4/0.0	245.8	159.4	255.4

Proposed traces coincide. Dashed lines are reference limits and dotted lines are load events. At ±15 A, Proposed PF recovery is 65.8/68.9 ms at 100 A/s and 57.7/55.4 ms at 500/2000 A/s. Q settling: $|Q-Q_{ref}| \le 80$ var until next event/end - all events in the supplement. F15/500 last exceeds 80 var at 1.3922 s and enters the band at 1.3923 s, giving 392.3 ms after L3 but only 7.7 ms before D. This does not prove or cause

long-run convergence or a threshold-sensitive finite-window setting. A PF recovery of 0 ms does not necessarily mean that the Q is settling. The downstream slew limiter is not tracked with outer-PI clamping on. At 1.20–1.28 s, phase RMS 6.339/10.745 A (mean) (1-μs samples) and fundamental apparent power 4.405/7.763 kVA (sum of phase Vrms × Irms) are within ±15 A Proposed/Fixed-Q. The converter-side resistance is 0.05 Ω, which dissipates RΣIrms2 = 6.027/17.317 W (excluding the other RL section, RC loss, and semiconductor/DC loss). Common-target superiority/total-efficiency claims are blocked by different targets.

RC-only keeps Breaker1 closed, blocks gates and isolates the VSC with a 10-MΩ snubber; converter peak after 0.1 s is 31.112 μA (<1 mA), RMS window is ≈22.000 μA. Measured PF is 0.984452/0.944331/0.984452, versus 0.98445/0.94433 when RL1 is included after L2/L3. Passive effects on PF also have effects on Qs, which are separated from VSC compensation in Table 11. RC-only reduces measured Q by 1.396 kVAr (4.499 to 3.103), versus 1.955 kVAr when RL1 is neglected. The RC branch carries 14.42 A rms, and analytically contributes 9.387 kW and −1.398 kVAr (with the first RL section contributing +0.588 kVAr). The earlier nominal 0.989/0.951 did not include RL1, so the computed PF for Loads 1–2 and Q for Loads 1–3 differ slightly.

Table 11. Diagnostic decomposition; A/B/C = 0.70–0.78/1.20–1.28/1.80–1.88 s

Metric/Window	OFF	RC-Only	Fixed-Q	Proposed
PF/A	0.871670	0.984452	1.000000	0.989939
Q/A	4.499	3.103	0.003	2.494
RMS/A	—	2.200e-05	4.739	1.139
THD20/A	0.000103	1.43e-06	1.267596	1.117924
PF/B	0.791353	0.944331	1.000000	0.990148
Q/B	8.499	7.103	0.010	2.932
RMS/B	—	2.200e-05	10.745	6.339
THD20/B	0.000066	9.05e-07	1.147581	1.005491
PF/C	0.871697	0.984452	1.000000	0.990095
Q/C	4.499	3.103	-0.011	2.468
RMS/C	—	2.200e-05	4.753	1.170
THD20/C	0.000083	1.02e-08	1.274437	1.124527

Note: Power factor (PF); root mean square (RMS).

6.5 Complexity and limits of validation shared

Powers, PLL, limits and PWM-reference adds 1 multiplication per update; transformations; PI loops. Its constant arithmetic complexity does not need to be optimized or trained. Execution time, memory and embedded operation are unmeasured. Validation includes balanced linear loads, shared environmental inputs. Nonlinear/unbalanced loads, isolated PV disturbances, reverse flow, MPPT efficiency, SOC, DC regulation, hardware verification, broad sensitivity, global stability and practical sizing remain unverified. Zero d-axis reference does not establish PV dispatch.

7. CONCLUSIONS

$Q_{s,ref}$ = 0.1425 Ps maintained PF near 0.99 with shared PI loops, whereas the fixed-zero-Q benchmark recovered faster and approached unity PF. The proposed method's lower aggregate target error at ±10 A reflects different targets and current-limit feasibility, not control-law superiority. Its potential benefit is lower converter current for the 0.99 target (6.339 versus 10.745 A rms in matched ±15 A logs), which establishes neither superiority at a common target nor lower total losses. The STATCOM-off baseline has near-zero THD20, and H2 depends on carrier phase and inner-loop sampling, so THD20 values do not indicate harmonic mitigation. RC-only operation gives PF 0.984452/0.944331/0.984452, so in the Load 2 and post-disconnection windows the VSC adds little; passive-branch effects must be separated from VSC compensation. Full-model tuning and stability analysis, practical sizing, DC-link validation, isolated PV disturbances, nonlinear/unbalanced loads and experimental verification remain open.

REFERENCES

[1] Muteri, V., Cellura, M., Curto, D., et al. (2020). Review on life cycle assessment of solar photovoltaic panels. Energies, 13(1): 1-38. https://doi.org/10.3390/en13010252

[2] Allouhi, A., Rehman, S., Buker, M.S., Said, Z. (2022). Up-to-date literature review on solar PV systems: Technology progress, market status and R&D. Journal of Cleaner Production, 362: 132339. https://doi.org/10.1016/j.jclepro.2022.132339

[3] Antar, R.K., Suliman, M.Y., Saleh, A.A. (2021). Harmonics resonance elimination technique using active static compensation circuit. Bulletin of Electrical Engineering and Informatics, 10(5): 2405-2413. https://doi.org/10.11591/eei.v10i5.3148

[4] Salem, W.A.A., Gabr Ibrahim, W., Abdelsadek, A.M., Nafeh, A.A. (2022). Grid connected photovoltaic system impression on power quality of low voltage distribution system. Cogent Engineering, 9(1): 2044576. https://doi.org/10.1080/23311916.2022.2044576

[5] IEEE Standard for Harmonic Control in Electric Power Systems, IEEE Std 519-2022, Aug. 2022.

[6] Yazdani, A., Iravani, R. (2010). Voltage-Sourced Converters in Power Systems: Modeling, Control, and Applications. John Wiley & Sons. https://doi.org/10.1002/9780470551578

[7] Patel, N., Gupta, N., Babu, B.C. (2020). Photovoltaic system operation as DSTATCOM for power quality improvement employing active current control. IET Generation, Transmission & Distribution, 14(17): 3518-3529. https://doi.org/10.1049/iet-gtd.2019.1487

[8] Alkhayyat, M.T., Khalaf, L.A., Suliman, M.Y. (2023). Adaptive control for power management based on renewable energy. Przegląd Elektrotechniczny, 99. https://doi.org/10.15199/48.2023.12.19

[9] Pal, R.S., Mukherjee, V. (2022). Student psychology and social group optimizations based modified synchronous reference frame control topology for PV-DSTATCOM. Electric Power Systems Research, 213: 108677. https://doi.org/10.1016/j.epsr.2022.108677

[10] Ibrahim, W.K., Alkhayyat, M.T., Suliman, M.Y. (2025). Unbalanced voltage enhancement based on STATCOM for distribution network integrated with renewable energy. International Journal of Electrical and Electronics Research, 13(3): 572-579. https://doi.org/10.37391/IJEER.130322

[11] Liang, H., Minfu, A., Zhang, Y., et al. (2025). Discrete-time deadbeat control for STATCOMs based on DQ

reference frame: A high-speed, tuning-free strategy for reactive current regulation. Frontiers in Energy Research, 13: 1667565. https://doi.org/10.3389/fenrg.2025.1667565

[12] Basnet, H., Roinila, T. (2024). Combining proportional-integral, deadbeat, and repetitive current controllers in energy-storage-equipped STATCOM application. IEEE Access, 12: 99499-99507. https://doi.org/10.1109/ACCESS.2024.3419444

[13] Li, J., Ye, C., Xiao, M., et al. (2026). Fast adaptive reactive-power compensation control for renewable power plants considering dynamic active-power–voltage coupling. Energies, 19(17): 3945. https://doi.org/10.3390/en19173945

[14] Pandey, S.A., Kallamadi, M., Shah, K. (2025). Cascaded AC-DC voltage control to provide reactive power support for the PV-driven grid-tied synchronverter. International Journal of Circuit Theory and Applications, 53(6): 3778-3786. https://doi.org/10.1002/cta.4297

[15] IEEE Standard for Interconnection and Interoperability of Distributed Energy Resources with Associated Electric Power Systems Interfaces. IEEE Std 1547-2018, Apr. 2018. https://standards.ieee.org/ieee/1547/5915.

[16] Ali, Z., Abbas, S.Z., Mahmood, A., Ali, S.W., Javed, S.B., Su, C.L. (2023). A study of a generalized photovoltaic system with MPPT using perturb and observer algorithms under varying conditions. Energies, 16(9): 3638. https://doi.org/10.3390/en16093638

[17] Ghribi, M.E.B., Garcia-Gutierrez, L., Ternifi, Z.E.T., Zheng, Z., Bachir, G., Aillerie, M. (2024). Tracking the maximum power point of solar panels through direct estimation of optimum voltage with temperature. Clean Energy, 8(4): 135-146. https://doi.org/10.1093/ce/zkae044

[18] Katche, M.L., Makokha, A.B., Zachary, S.O., Adaramola, M.S. (2023). A comprehensive review of maximum power point tracking (MPPT) techniques used in solar PV systems. Energies, 16(5): 2206. https://doi.org/10.3390/en16052206

[19] Malkawi, A.M., Odat, A., Bashaireh, A. (2022). A novel PV maximum power point tracking based on solar irradiance and circuit parameters estimation. Sustainability, 14(13): 7699. https://doi.org/10.3390/su14137699

[20] Alkhayyat, M.T., Suliman, M.Y., Aiwa, F.F. (2021). PQ & DQ based shunt active power filter with PWM & hysteresis techniques. Przegląd Elektrotechniczny, 97. http://doi.org/10.15199/48.2021.09.17

NOMENCLATURE

C_b	DC-side capacitance, F
D, ΔD	Boost duty ratio and perturbation step dimensionless
e_Q	Source reactive-power error, var
e_d, e_q	d- and q-axis current errors, A
f_{sw}	Switching frequency, Hz
G	Solar irradiance, W/m²
i_d, i_q	Converter d- and q-axis currents, A
i_d^*, i_q^*	Converter current references, A
i_{sd}, i_{sq}	Source d- and q-axis currents, A
i_L, i_{dc}	Boost-inductor and net DC-node currents, A
I_{PV}, I_{mpp}, I_{sc}	PV current, MPP current and short-circuit current, A
k	Discrete sample index, dimensionless
K_p, K_i	PI proportional and integral gains; units depend on loop signal scaling
L_b, L_f	Boost and interfacing inductances, H
N_{pv}	Number of PV modules, dimensionless
P, P_s, P_{PV}	Active power, source active power and PV power, W
PF, PF_{ref}	Power factor and reference, dimensionless
Q, Q_s, $Q_{s,ref}$	Reactive power, source reactive power and reference, var
R_f	Interfacing resistance, Ω
s(k)	P&O perturbation direction, dimensionless
SOC	Battery state of charge, %
T	PV-cell temperature, °C
T_s	Sampling period, s
u_d, u_q	d- and q-axis PI voltage outputs, V
v_d, v_q	PCC d- and q-axis voltages, V
V_{cd}^*, V_{cq}^*, V_{c0}^*	Converter reference voltages, V
V_{dc}, V_{PV}	DC-link and PV voltages, V
V_{mpp}, V_{oc}	MPP and open-circuit PV voltages, V
ΔP, ΔV	Sample-to-sample PV power and voltage changes, W and V
ω	Grid angular frequency, rad/s
$K_{p,Q}$, $K_{i,Q}$	Outer reactive-power PI gains
$K_{p,c}$, $K_{i,c}$	Inner current PI gains
$T_{s,Q}$	Outer-loop sampling period, s
PF_s	Source power factor, dimensionless
Subscripts	d/q: synchronous axes; s: source; c: converter; ref: reference; mpp: maximum power point; oc/sc: open/short circuit; pv: photovoltaic
Superscript *	Command or reference value